Virus surface-inspired ligand-switchable nanoparticles enable sequential drug delivery for improved oral insulin therapy

Tiantian Yang
  Shanghai Institute of Materia Medica

Aohua Wang
  Shanghai Institute of Materia Medica

Di Nie
  shanghai institue of materia medica

Weiwei Fan
  shanghai institue of materia medica

Xiaohe Jiang
  Shanghai Institute of Materia Medica

Miaorong Yu
  Shanghai Institute of Materia Medica

Shiyan Guo
  Shanghai Institute of Materia Medica

Chunliu Zhu
  Shanghai Institute of Materia Medica, Chinese Academy of Sciences

Gang Wei
  School of Pharmacy, Fudan University   https://orcid.org/0000-0002-9600-0982

Yong Gan（✉ ygan@simm.ac.cn）
  shanghai institue of materia medica   https://orcid.org/0000-0002-4579-994X

Article

Virus surface-inspired ligand-switchable nanoparticles enable sequential drug delivery for improved oral insulin therapy

Tiantian Yang[1,2], Aohua Wang[1,2], Di Nie[1,2], Weiwei Fan[1,2], Xiaohe Jiang[1,2], Miaorong Yu[1,2], Shiyan Guo[1], Chunliu Zhu[1], Gang Wei[3*], Yong Gan[1,2,4*]

[1]State Key Laboratory of Drug Research, Shanghai Institute of Materia Medica, Chinese Academy of Sciences, Shanghai 201203, China

[2]University of Chinese Academy of Sciences, Beijing 100049, China

[3]Key Laboratory of Smart Drug Delivery, Ministry of Education, Department of Pharmaceutics, School of Pharmacy, Fudan University, Shanghai 201203, China

[4]NMPA Key Laboratory for Quality Research and Evaluation of Pharmaceutical Excipients, National Institutes for Food and Drug Control, Beijing 100050, China

Corresponding author: Gang Wei (weigang@shmu.edu.cn), Yong Gan (ygan@simm.ac.cn)

Abstract

Mutual interference between surface ligands on multifunctional nanoparticles remains a significant obstacle to achieving the optimal drug-delivery efficacy. Inspired by viruses that modulate surface proteins conformation to enable sequential display of diverse functions, we develop ligand-switchable nanoparticles modified with a pH-responsive stretchable cell-penetrating peptide (Pep) and a liver-targeting moiety (Gal) (Pep/Gal-PNPs). The acidic environments encountered after oral administration trigger the extension of Pep from the surface in a virus-like manner, enabling Pep/Gal-PNPs to efficiently traverse intestinal barriers. Subsequently, Gal is exposed by Pep folding at physiological pH, thereby allowing the specific targeting of Pep/Gal-PNPs to the liver. As a proof-of-concept, insulin-loaded Pep/Gal-PNPs are fabricated which exhibit effective intestinal absorption and excellent hepatic deposition of insulin. Crucially, Pep/Gal-PNPs increase hepatic glycogen production by 7.2-fold, contributing the maintenance of glucose homeostasis for effective diabetes management. Overall, this study provides a promising approach to achieve full potential of diverse ligands on multifunctional nanoparticles.

Introduction

The surface functionalization of nanoparticles with various types of ligands with chemical or biological activity is a powerful tool for efficient drug delivery. These multifunctional nanoparticles have significant potential for overcoming complex physiological barriers and increasing the targeting efficiency of encapsulated drugs. This task is difficult to accomplish with a single ligand[1, 2]. For example, the covalent modification with RGD peptides and transferrin (Tf) ligands enables nanoparticles to transit across tumor vascular barriers and enhance the cellular uptake of drugs, respectively, leading to better antitumor efficacy[3]. However, mutual interference between diverse surface ligands would sterically hinder binding to receptors, ultimately compromising their functions[4, 5] and resulting in low efficacy of multifunctional nanoparticles[6, 7]. Therefore, there remain a significant challenge related to the surface multifunctionalization of nanoparticles, which substantially determines the efficiency of *in vivo* drug delivery.

Several strategies have emerged in recent decades to address the challenge by improving synergism of diverse ligands or controlling the presentation of specific ligands. One such strategy is to optimize the relative length, ratio, and density of dual-targeting ligands on nanoparticles by screening for the optimal formulation[8, 9]. An alternative strategy involves utilizing enzyme-responsive linkers to anchor one ligand on nanoparticles and cleaving the linker by specific enzymes to expose another ligand, enabling it to exert function at the target site[10, 11]. In addition, polyhistidine, a pH-sensitive molecular chain actuator, has also been applied to selectively expose conjugated functional moieties in response to acidic environments[12, 13]. Although these strategies have aimed to improve the targeting efficiency of nanoparticles, there still remains a major bottleneck in fully realizing the multiple functions of various ligand-modified nanoparticles.

Viruses, as natural delivery vectors, have evolved complex strategies to coordinate diverse surface proteins (also known as spike proteins) by responsively modulating their conformations, thereby enabling sequential functions that support efficient invasion[14]. Influenza A viruses (IAVs), for example, are studded with neuraminidase (NA) and hemagglutinin (HA) spikes that allow them to overcome mucus barriers and bind host cells[15, 16]. After binding, HA transforms from a folded (closed state) to a stretched (open state) conformation in the acidic endosomal compartment, which

67 mediates IAV penetration through membrane fusion with host cells[17]. Moreover, such

68 conformational changes in spike proteins have also been observed in numerous

69 enveloped viruses, such as coronaviruses[18, 19]. Therefore, the unique surface properties

70 of viruses spur the innovation of multifunctional nanoparticles that could realize the

71 full potential of diverse ligands in a virus-like manner.

72 To minimize mutual interference between ligands and improve the performance of

73 multifunctional nanoparticles, herein, inspired by the unique surface features of

74 viruses, we develop ligand-switchable poly (lactic-co-glycolic acid) (PLGA)

75 nanoparticles modified with a pH-triggered stretchable cell-penetrating peptide (Pep)

76 and a hepatic targeting moiety (galactose, Gal) (Pep/Gal-PNPs). After the oral

77 administration of Pep/Gal-PNPs, Pep adopts a stretched conformation and extends

78 from the surface in acidic environments, similar to viral spike proteins, mediating the

79 efficient traversal of intestinal barriers. Subsequently, upon entering systemic

80 circulation, Gal is exposed on the surface after Pep folds at physiological pH, thereby

81 specifically guiding Pep/Gal-PNPs to the liver (Figure 1). Since oral insulin delivery

82 requires the stepwise processes of traversing intestinal barriers and targeting the liver

83 to restore the liver–periphery insulin gradient and correct glucose metabolism defects

84 in the context of diabetes[20], as a proof-of-concept, we apply the Pep/Gal-PNPs for oral

85 insulin therapy in this study. The *in vivo* results indicate that insulin-loaded Pep/Gal-

86 PNPs not only elicit significant hypoglycemic effects but also promote hepatic

87 glucose sequestration and glycogen storage in diabetic rats, which show similar

88 glucose utilization as normal rats. In summary, this work presents a promising

89 alternative to recent attempts at the surface multifunctionalization of nanocarriers,

90 which is anticipated to be applied for a broad range of scenarios, such as oral delivery

91 of biomacromolecules and targeting delivery of antitumor drugs, playing a significant

92 role for improving their *in vivo* therapeutic efficacy.

93

94 **Results**

95 **Preparation and characterization of Pep and PLGA-based functional polymers.**

96 To prepare the multifunctional nanoparticles, the Pep and PLGA-conjugated

97 functional polymers, including PLGA-Pep and PLGA-PEG-Gal, were synthesized and

98 characterized. The Pep $R_6G_5(HE)_{10}$, which consists of arginine (R), glycine (G), and

99 histidine–glutamic acid (HE) repeats, is sensitive to environmental pH[21]. In acidic

100 environments (pH < 7), the Pep was in the open state with a theoretical length of

101 10.85 nm, whereas it switched to a closed state under physiological conditions (pH

102 ~7.4), with an estimated length of 7.00–7.88 nm depending on the folding pattern

103 (Figure 2a), according to previous studies[22]. The synthesized Pep was validated by

104 mass spectrometry (Figure 2b) and proton nuclear magnetic resonance (^{1}H NMR)

105 (Supplementary Fig. 1). Then, the pH-triggered conformational changes of Pep were

106 confirmed by circular dichroism (CD). The spectra revealed that Pep adopted a

107 random coil conformation, with the minimum absorption at 198 nm, and underwent

108 noticeable changes as the pH increased (Figure 2c). The ratio of β-sheet in the

109 secondary structure of Pep was estimated to increase from 11.9% to 26.5% when pH

110 increased from 6.8 to 7.4 by analyzing the CD spectra using Spectra Manager

111 software. As the β-sheet is the most common structure in the folding pattern of

112 proteins and peptides[23], the results indicated that Pep folded at physiological pH.

113 Furthermore, fluorescence resonance energy transfer (FRET) technique with the

114 Edans (fluorophore) and Dabcyl (quencher) pair was used to confirm the structural

115 changes of Pep in response to pH. There was a significant overlap between the Edans

116 emission spectrum and the Dabcyl absorption spectrum in the pH range of 3.0-8.0

117 (Supplementary Fig. 2), demonstrating that Dabcyl could absorb the fluorescence

118 emitted by Edans. Subsequently the Edans and Dabcyl were conjugated to the amino

119 acid side groups of N- and C-termini of Pep, respectively; the fluorescence intensity

120 of Edans decreased sharply when the pH increased from 6.8 to 7.4 (Figure 2d),

121 indicating that the two ends of Pep became closer upon adopting a folded

122 conformation at physiological pH. These results suggested that Pep underwent pH-

123 responsive conformational changes similar to viral spike proteins (e.g.,

124 hemagglutinin[17] and coronavirus spike glycoproteins[14]), with a stretched conformation

125 at acidic pH and a folded one at physiological pH. Moreover, we also studied changes

126 in activity of Pep in response to pH and results revealed that Pep exhibited a potent

127 hemolytic effect at pH < 7.0 but was inactive at physiological pH, indicating that Pep

128 was activated in a pH-dependent manner (Supplementary Fig. 3).

129 Subsequently, PLGA-conjugated functional polymers were further synthesized. A

130 cysteine was added to the C-termini of Pep to enable conjugation with maleimide-

131 capped PLGA (PLGA-Mal), thus creating PLGA-Pep polymers (Figure 2e). The

132 maleimide peak at 6.8 ppm in the ^{1}H NMR spectrum disappeared after conjugation

133 with Pep (Figure 2f), indicating the successful synthesis of PLGA-Pep polymers. To

134 selectively expose the other functional ligand (Gal) when Pep folded, polyethylene

135   glycol (PEG, MW 1.0 kDa) with an estimated length of 8.10 nm[8] was used as the

136   linker. The PEG chain was first conjugated with Gal and then coupled with PLGA-

137   COOH through an amidation reaction to obtain PLGA-PEG-Gal polymers (Figure 2g).

138   The intermediate product, PEG-Gal polymers, was monitored via ^{1}H NMR

139   (Supplementary Fig. 4), and the structure of PLGA-PEG-Gal was confirmed by the

140   representative PEG methylene signal at 3.6 ppm in the final spectrum (Figure 2h).

141   **Preparation and characterization of Pep/Gal-PNPs.** The PLGA nanoparticles

142   (PNPs) functionalized with various ligands were prepared through a double emulsion

143   and solvent evaporation method, as previously reported[24]. The modification rates for

144   the Pep and Gal ligands on nanoparticles were both approximately 5%

145   (Supplementary Table S1). The switchable surface properties of Pep/Gal-PNPs were

146   first investigated by dynamic light scattering (DLS) to determine the hydrodynamic

147   diameter and zeta potential at different pH. The results showed that the size of PNPs

148   increased significantly after ligand modification (Figure 3a). To specifically evaluate

149   the contribution of Pep to particle size, we also determined the diameter of Pep-

150   modified PNPs (Pep-PNPs). As expected, the diameter of Pep-PNPs decreased by

151   approximately 20 nm as the pH increased from 6.8 to 7.4 (Figure 3a), suggesting that

152   Pep folded at physiological pH. Although the size of Pep/Gal-PNPs decreased only

153   slightly as the pH increased due to the presence of PEG-Gal on the surface, the

154   observed differences in size under different pH conditions revealed the switchable

155   nature of the dual surface ligands (Figure 3a). As another measure of Pep/Gal-PNP

156   surface properties, the zeta potential was determined. For Pep-PNPs and Pep/Gal-

157   PNPs, the zeta potential sharply transitioned from positive to negative when the pH

158   increased from 6.8 to 7.4 (Figure 3b). By contrast, that of PNPs remained

159   approximately -35 mV regardless of pH (Figure 3b). As a previous study showed that

160   the cationic arginine in Pep can be neutralized by anionic glutamic acid at pH 7.4[25],

161   we hypothesized that changes in electrostatic interactions between the amino acids of

162   Pep might underlie the charge reversal of nanoparticles. Moreover, the morphologies

163   of PNPs, Pep-PNPs and Pep/Gal-PNPs were observed by cryogenic transmission

164   electron microscopy (cryo-TEM). All the nanoparticles showed spherical

165   morphologies with uniform size (Figure 3c).

166   To further elucidate the switchable nature of the surface ligands, the ligand corona

167   around the nanoparticles was directly observed by atomic force microscopy (AFM).

168   We detected the changes in individual immobilized nanoparticles under different pH

conditions by scanning the same position on the silica substrate and found that the diameter of Pep-PNPs was smaller at pH 7.4 than at pH 6.8 (Figure 3d, top row); specifically, the thickness of the Pep corona decreased by approximately 8 nm (from 25.86 ± 2.54 nm to 17.08 ± 0.60 nm) as the pH increased. By contrast, the ligand corona around Pep/Gal-PNPs decreased slightly over the same pH shift (Figure 3d, bottom row), which was consistent with the DLS results. Moreover, no significant changes were detected in the size of Gal-PNPs under different pH conditions; the thickness of PEG-Gal corona around nanoparticles remained in the range of 21–23 nm (Supplementary Fig. 5). Therefore, the AFM results confirmed that Pep underwent pH-responsive structural changes, suggesting that multifunctional Pep/Gal-PNPs featured switchable ligands with similar surface properties as viruses. Furthermore, we investigated the activity of Pep after decoration on Pep/Gal-PNPs, and results indicated it still retained the pH-dependent hemolytic effect (Supplementary Fig. 6). In contrast, PNPs exhibited relatively low hemolysis at all pH values (Supplementary Fig. 6).

Insulin, a protein drug widely used for the treatment of diabetes, was selected as the model drug in this study. The insulin entrapment efficiency and loading capacity of Pep/Gal-PNPs were determined to be 48.1% and 7.9%, respectively (Supplementary Table S1). Then, to investigate Pep/Gal-PNP stability after oral administration, the nanoparticles were incubated in PBS, simulated gastric fluid (SGF) or simulated intestinal fluid (SIF) with digestive enzymes for 4 h. The results showed that the relative size and dispersity of Pep/Gal-PNPs were not significantly different in SGF and SIF compared with that in PBS (Supplementary Fig. 7). Moreover, Pep/Gal-PNPs showed sustained insulin release *in vitro*, with approximately 23% of insulin released in 4 h (Supplementary Fig. 8a), and CD results demonstrated that the released insulin still retained a similar structure as native insulin (Supplementary Fig. 8b). Overall, these results indicated that Pep/Gal-PNPs could remain stable in the harsh gastrointestinal environment without premature release of encapsulated insulin.

Overcoming the mucus barrier. After being subjected to the harsh gastrointestinal environment, the next barrier encountered by Pep/Gal-PNPs is the mucus lining of the intestines, which must be crossed to reach the apical side of the intestinal epithelium[26]. Therefore, the ability of nanoparticles to penetrate mucus was investigated using HT29-MTX-E12 (E12) cells that secrete abundant mucus. Pep/Gal-PNPs exhibited strong fluorescence at the lower layer of mucus at pH 6.8 and 7.4 (Supplementary Fig.

9), suggesting the efficient mucus-penetrating ability. Given the observed ability of Pep/Gal-PNPs to penetrate the mucus barrier, the next obstacle that we interrogated was cellular uptake.

Pep/Gal-PNPs uptake by Caco-2 cells. To begin our cellular uptake analysis of Pep/Gal-PNPs, we first evaluated the cytotoxicity of these nanoparticles on human colorectal adenocarcinoma cells (Caco-2), and found no negative impact at concentrations of 0.05–1 mg/mL (Supplementary Fig. 10). Therefore, subsequent studies were conducted in that concentration range. To further ascertain the contribution of particular attributes of ligand-switchable Pep/Gal-PNPs, non-switchable nanoparticles with the cell-penetrating segment of Pep (CPP, R_6) and Gal (CPP/Gal-PNPs) were prepared and employed as a comparator (Supplementary Table S1). Importantly, CPP alone and CPP/Gal-PNPs showed potent, pH-insensitive hemolytic activity (Supplementary Fig. 11). Studies on cellular uptake of nanoparticles by Caco-2 cells at pH 6.0 to 8.0 indicated that Pep/Gal-PNP internalization increased markedly as the pH decreased, while PNP and CPP/Gal-PNP internalization was consistent across the pH gradient (Supplementary Fig. 12). Given these results, we compared the cellular uptake efficiency of nanoparticle at pH 6.8 and 7.4. Confocal laser scanning microscopy (CLSM) images revealed stronger fluorescence signals for CPP/Gal-PNPs and Pep/Gal-PNPs than PNPs at pH 6.8, whereas Pep/Gal-PNP fluorescence decreased markedly at pH 7.4, in contrast with no change in the other groups (Figure 4a). The quantitative analysis results revealed that cellular uptake of insulin in Pep/Gal-PNPs was 2.6-fold higher at pH 6.8 than at pH 7.4 and was almost 4.7-fold higher than that of PNPs (Figure 4b). In contrast, free insulin could hardly be taken up by cells (Supplementary Fig. 13). These results indicated that Pep was exposed on the surface in response to mildly acidic pH and promoted the endocytosis of Pep/Gal-PNPs, leading to the intracellular delivery of insulin.

To better understand the effect of surface ligands on cellular uptake, the endocytosis mechanism of Pep/Gal-PNPs at different pH values was investigated. The uptake of Pep/Gal-PNPs was significantly decreased at 4 °C, suggesting that the endocytosis pathway was energy-dependent (Supplementary Fig. 14). To further interrogate the mechanism, the endocytic inhibitors amiloride (macropinocytosis), chlorpromazine (clathrin-mediated endocytosis), and filipin (caveolae-mediated endocytosis) were used. Pep/Gal-PNP internalization by Caco-2 cells markedly decreased (to 49.6%)

upon pretreatment with amiloride compared to control at pH 7.4, whereas no significant difference was observed at pH 6.8 (Supplementary Fig. 14). Compared to the control, chlorpromazine significantly decreased the uptake of Pep/Gal-PNPs to 39.7% at pH 6.8 and 61.6% at pH 7.4, respectively. By contrast, filipin had negligible effects on Pep/Gal-PNP uptake (Supplementary Fig. 14). These results revealed that ligand-switchable Pep/Gal-PNPs mainly adopted clathrin-dependent endocytosis pathway at pH 6.8 mediated by the surface-exposed Pep, whereas macropinocytosis predominated once Pep folded and got inactivated at physiological pH.

Intracellular trafficking and transcytosis of Pep/Gal-PNPs. After entering cells, nanoparticles are typically transferred from endosomes to lysosomes for degradation[27]. Thus, to evaluate whether Pep/Gal-PNPs undergo intracellular lysosomal degradation, we used CLSM to investigate their colocalization with lysosomes. Interestingly, all the PNP, CPP/Gal-PNP, and Pep/Gal-PNP groups showed weak colocalization signals with lysosomes after incubation for 2 h (Figure 4c), suggesting the capture of few nanoparticles. The hemolytic assay demonstrated the membrane-disrupting capabilities of CPP/Gal-PNPs and Pep/Gal-PNPs. Moreover, histidine protonation in Pep could also promote the release of Pep/Gal-PNPs from the lysosome[28]. Overall, these results indicated that Pep/Gal-PNPs could escape from lysosomal during intracellular trafficking, thereby protecting encapsulated insulin from degradation.

As Pep/Gal-PNPs appeared to remain intact intracellularly, the transcytosis efficiency of insulin by different formulations was next investigated. Pep/Gal-PNPs exhibited the highest apparent permeability coefficient (P_{app}) ($9.62 \pm 1.34 \times 10^{-6}$ cm/s) at pH 6.8, representing a 2.9-fold increase over that at pH 7.4 (Figure 4d). In contrast, the P_{app} values of PNPs and CPP/Gal-PNPs were not significantly different at pH 6.8 and 7.4 (Figure 4d), and free insulin showed little transport across Caco-2 cells (Supplementary Fig. 13). The lack of a significant reduction in the transepithelial electrical resistance (TEER) of cells during transcytosis further confirmed that the nanoparticles underwent transcellular transport without opening of the tight junctions of cells (Supplementary Fig. 15). Together, the results suggested that ligand-switchable Pep/Gal-PNPs promoted transcytosis of encapsulated insulin under mildly acidic conditions.

We next ascertained whether Pep/Gal-PNPs maintained structural integrity after exiting cells. FITC and RITC were encapsulated simultaneously in Pep/Gal-PNPs (FITC/RITC@NP) which were then incubated with cells for 2 h. An intense FRET

spectrum was detected in the basolateral medium, suggesting that Pep/Gal-PNPs remained intact after exocytosis; this result was further confirmed by the cryo-TEM image (Figure 4e). After confirming the general structural integrity of transcytosed Pep/Gal-PNPs, we next aimed to determine if the Pep still reserved pH sensitivity. Thus, Edans- and Dabcyl-labeled Pep was used to prepare Pep/Gal-PNPs (Edans-Pep-Dabcyl-NP) which were incubated with cells and then collected from the basolateral medium. The emission intensity of these recovered Edans-Pep-Dabcyl-NP decreased markedly after the pH increased from 6.8 to 7.4 (Figure 4f), yielding similar results as the FRET assay of Pep. These results demonstrated that Pep/Gal-PNPs remained unchanged during transepithelial transport, increasing the possibility of subsequent site-specific targeting.

Selectivity of Pep/Gal-PNPs for hepatocytes. After verifying that Pep could facilitate uptake of Pep/Gal-PNPs by intestinal epithelium, we further explored the functions of Gal ligands. Asialoglycoprotein receptors (ASGPRs) expressed on hepatocytes can specifically recognize Gal residues[29]. Therefore, the human fetal hepatocytes (LO2 cells) which expressed high levels of ASGPRs (Supplementary Fig. 16), were used as cell model to study the interaction of Pep/Gal-PNPs with hepatocytes. Moreover, the Pep/Gal-PNPs exhibited negligible toxicity on LO2 cells (Supplementary Fig. 17). CLSM results indicated that Pep/Gal-PNPs exhibited strong fluorescence on LO2 cells regardless of pH (Figure 4g). However, upon preincubation of the cells with free Gal, Pep/Gal-PNP fluorescence decreased markedly at pH 7.4 but not at pH 6.8 (Figure 4g), indicating the important role of Gal in binding to LO2 cells. In contrast, the addition of Gal had no impact on PNP or CPP/Gal-PNP fluorescence at pH 6.8 or 7.4 (Supplementary Fig. 18); it might be ascribed to the non-selective cell-penetrating ability of CPP, which would enable the deposition of CPP/Gal-PNPs on hepatocytes regardless of pH. Then, we investigated the colocalization of Pep/Gal-PNPs with ASGPRs on LO2 cells and found greater colocalization at pH 7.4 than at pH 6.8 (Figure 4h). Accordingly, these results demonstrated that physiological pH triggered ligand switching on the Pep/Gal-PNP surface to present Gal, which specifically bound with ASGPRs on hepatocytes. As the hepatocyte is the main site for endogenous insulin to take effect[30], Pep/Gal-PNPs could specifically deliver encapsulated insulin to the aimed sites.

Intracellular signaling upon Pep/Gal-PNPs binding. The cellular effects of insulin are initiated at the cell membrane by binding to the insulin receptor (IR), which can

305 stimulate the intracellular PI3K/AKT pathway and elicit the phosphorylation of AKT

306 (p-AKT)[31]. Thus, as an increase in intracellular p-ATK levels indicates the activation

307 of IR-related signaling pathways, we investigated p-AKT levels in LO2 cells to

308 evaluate the signaling potential of insulin delivered by Pep/Gal-PNPs. In this

309 experiment, LO2 cells exposed to insulin-loaded Pep/Gal-PNPs at pH 7.4 showed a

310 gradual increase over time in intracellular p-AKT levels, which reached the same

311 level as the free insulin group after 2 h of treatment (Figure 4i). We deduced that

312 insulin was continuously released from Pep/Gal-PNPs and activated downstream

313 intracellular pathways by binding to IR.

314 To further analyze the intracellular effects of insulin-loaded Pep/Gal-PNPs, modified

315 pulse-chase p-AKT assays[32] were conducted to determine the sustained effect of these

316 nanoparticles on LO2 cells, as previously reported. In this experiment, LO2 cells were

317 first pulsed with free insulin and insulin-loaded Pep/Gal-PNPs for 30 min, then

318 washed and chased by incubation in insulin-free DMEM. The results revealed that 4 h

319 after the Pep/Gal-PNPs were removed, the cells still expressed high p-AKT levels,

320 whereas p-AKT could not be detected in free insulin group after discarding the insulin

321 solution (Supplementary Fig. 19). These results demonstrated that intracellular AKT

322 phosphorylation is induced mainly by insulin released from cell-bound Pep/Gal-PNPs

323 due to the Gal–ASGPR interaction. In summary, the ligand-switchable Pep/Gal-PNPs

324 bound to LO2 cells via interactions between the exposed Gal and ASGPRs at

325 physiological pH, whereby they served as an insulin reservoir for the sustained

326 activation of intracellular IR-related signaling pathway (Figure 4j).

327 ***In vivo* intestinal absorption of Pep/Gal-PNPs.** Given these promising *in vitro*

328 results, we next investigated the advantageous properties of Pep/Gal-PNPs for

329 efficient drug delivery *in vivo*. To investigate intestinal absorption of Pep/Gal-PNPs,

330 the real-time transport of nanoparticles into intestinal villi of rat was studied using

331 two-photon microscopy (TPM), which offers higher imaging depth with less

332 photodamage[33]. After treatment for 30 min, much stronger Pep/Gal-PNP fluorescence

333 was observed in intestinal villi at pH 6.8 than at pH 7.4. By contrast, similar intense

334 CPP/Gal-PNP fluorescence was observed at pH 6.8 and 7.4 (Figure 5a). However,

335 nonfunctionalized PNPs consistently exhibited weak fluorescence signals in intestinal

336 villi (Supplementary Fig. 20). CLSM images of intestinal sections further confirmed

337 the greater intestinal absorption of Pep/Gal-PNPs at pH 6.8. FITC and RITC were

338 simultaneously encapsulated in Pep/Gal-PNPs, and colocalization of these two signals

revealed the structural integrity of these nanoparticles (Figure 5a). Quantitative analysis revealed that the relative integrated density of Pep/Gal-PNPs was 3.6-fold higher at pH 6.8 than at pH 7.4, but no significant difference was detected for CPP/Gal-PNPs (Figure 5b). These results confirmed the better intestinal absorption of intact Pep/Gal-PNPs at the simulated intestinal pH, which was conducive to further delivering encapsulated drugs to the specific target sites.

***In vivo* liver accumulation and selectivity of Pep/Gal-PNPs.** After crossing intestinal barriers, Pep/Gal-PNPs could enter systemic circulation via portal vein at physiological pH. Therefore, we further investigated the tissue distribution of Pep/Gal-PNPs *in vivo*. At 4 h after oral administration of FITC-labeled nanoparticles to rats, the Pep/Gal-PNP fluorescence intensity in liver homogenates was much higher than other organs (almost 72.1% of the total), which was 1.66-fold higher than that of CPP/Gal-PNP group (Figure 5c). Additionally, we imaged the organs of rats using an *in vivo* imaging system (IVIS) to directly observe the biodistribution of nanoparticles. Pep/Gal-PNPs showed relatively more intense fluorescence in the liver compared with other organs, whereas CPP/Gal-PNPs exhibited strong fluorescence in the liver, lungs, and spleen (Figure 5d). In contrast, PNPs exhibited weak fluorescence in all organs except the intestine (Supplementary Fig. 21), indicating limited nanoparticles transported across intestinal barriers. Overall, these results indicated that the Pep/Gal-PNPs mainly accumulated in the liver.

To further confirm that Pep/Gal-PNPs can specifically target the liver, the colocalization of nanoparticles with ASGPRs on hepatocytes in liver sections was detected using CLSM after immunofluorescence staining. Greater colocalization with ASGPRs was observed for Pep/Gal-PNPs than for CPP/Gal-PNPs (Figure 5e). The colocalization coefficient (R) was calculated to be 0.03 for CPP/Gal-PNP group and 0.32 for Pep/Gal-PNP group, representing a 10.7-fold increase. In contrast, PNPs exhibited weak fluorescence in liver sections with little colocalization signals (Supplementary Fig. 22). The limited colocalization of CPP/Gal-PNPs with ASGPR was mainly attributed to the non-selectivity of CPP, which compromised the targeting efficiency of Gal and allowed the nanoparticles to be captured by other liver cells (e.g., endothelial and Kupffer cells) and organs. In contrast, on the surface of Pep/Gal-PNPs, Gal was deshielded at physiological pH since Pep folded, enabling specific Gal binding to ASGPRs on hepatocytes.

***In vivo* ligand-switching features of Pep/Gal-PNPs.** To clarify the sequential

intestinal barrier-crossing and liver-targeting abilities of Pep/Gal-PNPs, we further studied *in vivo* surface ligand-switching on Pep/Gal-PNPs by applying the FRET technique. A FRET pair, the carboxyfluorescein (FAM) as the donor and the carboxytetramethylrhodamine (TAMRA) as the acceptor, was conjugated to amino acid side groups of N- and C-termini of Pep, respectively. The FRET pair-labeled Pep was further applied to prepare the Pep/Gal-PNPs (FR-Pep/Gal-PNPs). Rat intestine and liver segments were isolated at 2 h and 4 h, respectively, after the oral administration of FR-Pep/Gal-PNPs, and the FRET efficiency of the nanoparticles was detected. Although FR-Pep/Gal-PNPs exhibited strong fluorescence in the intestine, the FRET efficiency remained relatively low (approximately 11.6%) (Figure 5f), highlighting the stretched structure of the Pep. By contrast, the FRET efficiency of FR-Pep/Gal-PNPs was markedly increased in the liver, with a nearly 5-fold increase in efficiency compared with the intestine. Consistent with the *in vitro* results, the *in vivo* FRET findings further confirmed that Pep underwent structural changes in response to environmental pH along the oral route from the intestine to the liver, enabling the switching of surface functional ligands on Pep/Gal-PNPs.

Visualization of systemic delivery route of Pep/Gal-PNPs *in vivo*. To thoroughly examine *in vivo* delivery route of Pep/Gal-PNPs after oral administration, FITC-labeled Pep/Gal-PNPs were visualized in the intestine and liver of a living rat using confocal laser endomicroscopy (CLE). Widespread green fluorescence of Pep/Gal-PNPs was detected in small intestine villi 2 h after administration (Figure 6a, top row), indicating efficient intestinal absorption of the nanoparticles. After 4 h, marked Pep/Gal-PNP accumulation was observed in the liver, as indicated by the intense fluorescence (Figure 6a, bottom row). Moreover, Pep/Gal-PNP fluorescence was observed to gradually increase from blood vessels to hepatocytes in the deep scan images (Figure 6a, denoted by arrows). We speculated that fenestrations in liver sinusoidal endothelial cells[34] enabled Pep/Gal-PNPs to traverse hepatic vessels and reach hepatocytes. Collectively, these results confirmed that ligand-switchable Pep/Gal-PNPs could sequentially transit across intestinal barriers and accumulate in the liver to deliver insulin to hepatocytes.

***In vivo* hypoglycemic efficacy.** In culmination of seeing that the Pep/Gal-PNPs arrive at the liver and deliver insulin to hepatocytes, we further investigated whether these nanoparticles would lead to an effective physiological response. As an indicator of the pharmacodynamic (PD) profile of insulin-related formulations, the hypoglycemic

effect was evaluated in type I diabetic rats based on the blood glucose level (BGL) after dosing. The BGL of diabetic rats treated subcutaneously with free insulin dropped sharply to approximately 15.7% of the initial level at 3 h post-administration and then gradually returned to the basal level (Figure 6b). Notably, wild fluctuations in blood glucose can cause hypoglycemia, blindness, heart disease, and kidney failure[35]. In contrast, insulin-loaded nanoparticles yielded more moderate and prolonged hypoglycemic effects (Figure 6b). Among the three nanoparticle formulations, Pep/Gal-PNPs generated the most pronounced hypoglycemic effect, reaching a minimum BGL of 23.2% of the initial level at 8 h post-administration (Figure 6b). Moreover, the BGL of rats treated with Pep/Gal-PNPs remained within the normal range for 7 h (Supplementary Fig. 23). Correspondingly, Pep/Gal-PNPs were calculated to achieve the highest pharmacological availability (PA) of 10.1% (Supplementary Table S2).

Subsequently, the pharmacokinetic (PK) profiles of different formulations were investigated based on the serum insulin concentration over time. Consistent with the PD results, diabetic rats treated with subcutaneous insulin showed a sharp increase in peripheral serum insulin, which reached the maximum 1 h post-injection and rapidly decreased to baseline in the following 3 h (Figure 6c). Compared with the other nanoparticle formulations, Pep/Gal-PNPs achieved a considerably higher concentration of insulin at 4 h post-administration (Figure 6c) and reached the highest relative oral bioavailability of insulin at 7.7% (Table 1). Notably, this is one of the best results that we have seen in the literature of PLGA-based oral insulin nanoparticles[36].

***In vivo* hepatic glucose utilization studies.** It has been reported that direct delivery of insulin to the liver could promote hepatic glucose utilization and glycogen production in diabetes[20]. Therefore, we evaluated hepatic glycogen storage in diabetic rats treated with different formulations. Quantitative analysis results indicated that orally administered with insulin-loaded Pep/Gal-PNPs induced the highest level of liver glycogen synthesis, with a relative hepatic glycogen content (HGC) approximately 7.24-, 1.92- and 2.74-fold higher than that in the diabetic rats (D group), subcutaneous injection of insulin (INS group) and CPP/Gal-PNP group (Figure 6d). Surprisingly, the Pep/Gal-PNP group had a hepatic glycogen level similar to that in the normal rats (N group) (Figure 6d). Moreover, the glycogen synthesis in rats was directly observed by using periodic acid-Schiff (PAS) staining. The D group

presented depleted glycogen levels in the liver compared to N group, and this depletion was hardly improved by treatment with PNPs (Figure 6e). In contrast, large amounts of hepatic glycogen were detected in the Pep/Gal-PNP group compared with INS and CPP/Gal-PNP groups (Figure 6e).

Since the insulin-loaded Pep/Gal-PNPs largely accumulated in the liver, we further demonstrated that these nanoparticles elicited the highest portal serum insulin levels among the formulations (Supplementary Fig. 24). Notably, the area under the curve (AUC) of the portal serum insulin level in Pep/Gal-PNP group was 4.1-fold higher than in subcutaneous insulin group (Supplementary Table S3). These results demonstrated that the Pep/Gal-PNPs could promote hepatic glycogen production in diabetic rats through elevating intrahepatic insulin exposure. In summary, we developed the reasonable hypothesis that ligand-switchable Pep/Gal-PNPs underwent efficient intestinal absorption to enable the subsequent hepatic deposition of insulin, which replicated the endogenous insulin pathway to reestablish a high portal–periphery insulin gradient, thereby promoting the conversion of blood glucose into glycogen for storage and maintaining glucose homeostasis.

***In vivo* toxicity analysis.** Finally, the *in vivo* toxicity of the Pep/Gal-PNPs was assessed by monitoring the body weight of rats after the oral administration of nanoparticles every day for a week. In these studies, the administration dose of nanoparticles (1000 mg/kg) was about 20-fold higher than their effective dose (50 mg/kg). The results showed no significant differences in the body weight of rats in the experimental groups compared to the control group (Figure 6f). As an indicator of potential liver toxicity, serum alanine aminotransferase (ALT) and aspartate aminotransferase (AST) levels were detected in the experimental and control groups. Importantly, serum ALT and AST levels were within the normal range (ALT: 10 to 40 IU/L; AST: 50 to 150 IU/L)[37] for rats in all groups (Figure 6g, 6h). Moreover, hematoxylin and eosin (H&E) staining revealed no histological damage in the intestine or liver of experimental rats compared with control rats (Figure 6i, Supplementary Fig. 25). These results demonstrated that Pep/Gal-PNPs were biocompatible *in vivo* and thus suitable for oral insulin delivery.

Discussion

Drug delivery systems with multiple functions are required to traverse complex

physiological environments and target to specific sites. However, mutual interference (e.g., steric hindrance and electrostatic interactions) between surface ligands might be an important factor limiting their functionalities and thus resulting in low *in vivo* drug delivery efficiency of these multifunctional vehicles[5, 9]. Here, inspired by the unique surface properties of viruses[14, 17], we proposed a novel strategy to fully realize the functionalities of different ligands on nanoparticles. We rationally designed multifunctional nanoparticles (Pep/Gal-PNPs) with simultaneous modification of dual ligands. The Pep ligands on Pep/Gal-PNPs underwent conformational changes similar to viral spike proteins, extending from surface when at simulated intestinal pH (6.8) and folding at physiological pH (7.4), as demonstrated *in vitro* and *in vivo* studies. Moreover, the AFM results indicated the other Gal ligands on Pep/Gal-PNPs could be exposed on surface as the Pep folded at physiological pH. Therefore, by mimicking unique viral surface features, the dual functional ligands on Pep/Gal-PNPs switched in response to environmental pH. Although some nanoparticles with viral morphology or function have been developed[38], to the best of our knowledge, this is the first study to apply the distinctive surface functionalization features of viruses.

The ligand-switchable Pep/Gal-PNPs demonstrated the potential to sequentially exert functions of diverse surface ligands triggered by pH variations along the delivery route from intestine to the liver after oral administration. Meanwhile, the Pep/Gal-PNPs could maintain stability in the harsh physiological environment due to the protection of PEG layer. First, the Pep adopted a stretched conformation and got activated at simulated intestinal pH, which increased its exposure on the surface and promoted the intestinal absorption of Pep/Gal-PNPs. During intracellular trafficking, the Pep/Gal-PNPs could escape from lysosomal degradation. Therefore, Pep/Gal-PNPs exhibited high transepithelial transport efficiency. To confirm the *in vitro-in vivo* correlation, we also observed the efficient intestinal absorption of Pep/Gal-PNPs in a living rat by using the intravital two-photon microscopy. These studies demonstrated that Pep/Gal-PNPs could efficiently overcome the intestinal barrier which typically functions as the first line of defense to restrict nanoparticles from entering blood circulation[39, 40]. Then, after traversing the intestinal barriers, most of the nanoparticles are delivered to the portal vein, which harbors a physiological pH; therefore, Gal was deshielded on the surface of Pep/Gal-PNPs as Pep folded in this microenvironment. Although most nanoparticles inevitably reach the liver after oral administration, Pep/Gal-PNPs could selectively target hepatocytes through the

binding of Gal to ASGPRs on cells. The high liver-targeting efficiency of Pep/Gal-PNPs is comparable to that of previously reported Gal-modified nanoparticles[41]. The *in vivo* systemic trafficking of Pep/Gal-PNPs was also observed by endomicroscopic imaging, confirming the sequential intestinal barrier penetration and hepatic accumulation of these ligand-switchable nanoparticles. Taken together, the ligand-switchable nature of Pep/Gal-PNPs could realize the full potential of the dual surface ligands, ultimately delivering encapsulated drugs to the liver with high efficiency.

As a proof-of-concept, we utilized insulin as the model drug, and the ligand-switchable Pep/Gal-PNPs could enhance intestinal absorption of encapsulated insulin, further targeting delivery to hepatocytes. *In vivo* therapeutic assessments revealed that the insulin-loaded Pep/Gal-PNPs elicited a sustained and strong hypoglycemic response on diabetic rats. Moreover, the insulin-loaded Pep/Gal-PNPs could increase insulin deposition in the liver and restore the liver–periphery insulin gradient in diabetes. It has been reported that the liver is exposed to approximately 2- to 4-fold higher concentrations of endogenous insulin than peripheral tissues (such as brain and fat) under normal circumstances[42]. However, this physiological distribution would be disrupted by conventional subcutaneous injection of insulin which may lead to peripheral hyperinsulinemia and severe hypoglycemia[43]. In comparison, the Pep/Gal-PNPs could mimic the biodistribution of endogenous insulin through actively targeting insulin to the liver, showing advantageous for diabetes treatment.

Furthermore, we investigated the mechanism of action of the insulin-loaded Pep/Gal-PNPs on the liver. In this study, we showed that insulin-loaded Pep/Gal-PNPs could sustainably activate PI3K/AKT signaling pathway in hepatocytes. This intracellular signaling pathway is the primary pathway of insulin signaling transduction, which is involved in regulating glucose utilization and glycogen storage[44]. Therefore, these results reminded us that insulin-loaded Pep/Gal-PNPs had the potential to promote hepatic glycogen synthesis. To our knowledge, these findings are the first attempt to explicit the mechanism for the liver-targeting oral insulin therapy.

Correspondingly, our animal experiments demonstrated that the insulin-loaded Pep/Gal-PNPs not only effectively reduced BGL but also significantly promoted hepatic glycogen production in diabetic rats. Compared with the conventional subcutaneous injection of insulin, orally administered insulin-loaded Pep/Gal-PNPs showed greater efficacy in promoting liver to take up and store glucose as glycogen due to superior liver selectivity. Surprisingly, the hepatic glycogen level in Pep/Gal-

PNP-treated diabetic rats was similar to that in healthy rats, suggesting that this treatment could potentially correct defects in glucose metabolism in diabetes. Most recent studies of oral insulin therapy mainly focus on lowering blood glucose. However, dramatic fluctuations in BGLs are more deleterious than stable high glucose concentrations[45]. The liver glycogen plays a critical role in defending against hypoglycemia[46]. Whereas, hepatic glycogen storage is impaired in diabetes, which restricts the ability of hepatocytes to respond appropriately to glucose levels[20]. Therefore, Pep/Gal-PNPs have the potential to maintain glycemic homeostasis rather than merely lowering BGL in the context of diabetes. Outcomes of this study emphasize the importance of hepatic glycogen for diabetes management and the ligand-switchable Pep/Gal-PNPs may represent a significantly improved oral insulin therapy.

In summary, we have rationally developed ligand-switchable nanoparticles (Pep/Gal-PNPs) that realize the full potential of dual surface functionalities in response to environmental pH by mimicking unique surface features of viruses. Pep/Gal-PNPs sequentially overcome intestinal barriers and target insulin to the liver in response to variations in pH after oral administration, thereby promoting the production of hepatic glycogen to maintain glucose homeostasis as improved oral insulin therapy. Moreover, this study provides a promising strategy for the effective functionalization of nanocarriers with diverse ligands, which exhibit tremendous potential for a broad range of drug-delivery applications in the future, such as biomacromolecules and antitumor drugs.

Materials and Methods

Experimental reagents. Poly (D, L-lactide-co-glycolide)-carboxylic acid (PLGA-COOH, LA/GA molar ratio 50:50, Mw ~15,000 Da) was purchased from Daigang Biomaterial Co., Ltd. (Jinan, China) and the PLGA-maleimide (PLGA-Mal, LA/GA molar ratio 50:50, Mw ~15,000 Da) was synthesized by Ruixi Biological Technology Co., Ltd. (Xi'an, China). Diamino-poly (ethylene glycol) (NH_2-PEG-NH_2, Mw ~1,000 Da) was purchased from Ponsure Biological Technology Co., Ltd. (Shanghai, China). The pH-triggered stretchable cell-penetrating peptide (Pep) and FRET pair-labeled Pep was synthesized by BankPeptide Biological Technology Co., Ltd. (Hefei, China). Human insulin was the gift received from Novo Nordisk A/S. Fluorescein

isothiocyanate (FITC), 3-(4, 5-Dimethyl-2-thiazolyl)-2, 5-diphenyl-2H-tetrazolium bromide (MTT), rhodamine isothiocyanate (RITC), 2-(4-amidinophenyl)-6-indolecarbamidine dihydrochloride (DAPI), radioimmunoprecipitation assay (RIPA), Lyso-Tracker red and bicinchoninic acid (BCA) Protein Assay Kit were all purchased from Meilun Biotechnology Co., Ltd. (Dalian, China). Hoechst 33258, Hoechst 33342 and Alexa 647 labeled goat anti-rabbit IgG was purchased from Yeasen Biotechnology Co., Ltd. (Shanghai, China). Anti-ASGPR rabbit polyclonal antibody (pAb), anti-GAPDH mouse pAb, horseradish peroxidase (HRP)-conjugated goat anti-rabbit IgG, and HRP-conjugated goat anti-mouse IgG were all purchased from Sangon Biotechnology Co., Ltd. (Shanghai, China). Phospho-AKT (Ser473) rabbit monoclonal antibody (mAb) was purchased from Bimake Co., Ltd. (Houston, USA). Human insulin ELISA kits were purchased from Mercodia (Uppsala, Sweden), glycogen ELISA kits were purchased from Solarbio Science and Technology Co., Ltd. (Beijing, China) and ALT and AST assay kits were purchased from Nanjing Jiancheng Bioengineering Co., Ltd. (Nanjing, China). All the other chemicals were of analytical grade and were purchased from Sinopharm Chemical Reagent Co., Ltd. (Shanghai, China).

Cell culture. Caco-2 and LO2 cell lines were purchased from the American Type Culture Collection (Manassas, USA). HT29-MTX-E12 (E12) cell line was kindly provided by Novo Nordisk A/S (Denmark). Caco-2 and LO2 cells were maintained in Dulbecco's Modified Eagle medium (DMEM) with 5% (v/v) fetal bovine serum (FBS), 1% penicillin and streptomycin (100 IU/mL) at 37 °C in 5% CO_2. E12 cells were maintained in DMEM with 10% (v/v) FBS, 1% (v/v) nonessential amino acids, 1% penicillin and streptomycin (100 IU/mL) at 37 °C in 5% CO_2.

Animal care. Male Sprague–Dawley (SD) rats (200–220 g) were provided by the Animal Experiment Center of Shanghai Institute of Materia Medica (Shanghai, China). All animal experiments were conducted following the Institutional Animal Care and Use Committee (IACUC) guidelines of the Shanghai Institute of Materia Medica (IACUC code: 2020-05-GY-58). To induce type I diabetes, the rats were fasted overnight before studies but allowed free access to water, and then injected intraperitoneally with 10 mM streptozotocin at a dose of 65 mg/kg. The rats with fasting blood glucose levels higher than 300 mg/dL were regarded as diabetic.

Characterization of pH-triggered stretchable Pep. First, the synthesized Pep was dissolved in a mixture of water/acetonitrile/acetic acid (87:8:5) and analyzed via

electrospray ionization mass spectrometry (ESI-MS; QTRAP 4500, AB SCIEX, USA). Subsequently, 0.5 mg/mL Pep was incubated in PBS at pH 3.0, 5.0, 6.0, 6.8, 7.0, 7.4 and 8.0. The secondary conformation of Pep under different pH conditions was measured using circular dichroism (CD; J-810, JASCO, Japan) and analyzed by Spectra Manager software (JASCO, Japan). To investigate the structural changes in Pep in response to pH, Pep was modified at the N- and C-termini with 5-[(2-aminoethyl)amino]naphthalene-1-sulfonic acid) (Edans) and 4-(4-dimethylaminophenylazo)benzoic acid (Dabcyl) (a FRET pair), respectively. This FRET pair-labeled Pep was suspended in PBS at different pH values with the final concentration of 1 mg/mL, and the FRET emission of the Pep at 340 nm was measured by a microplate reader (Synergy H1, BioTek, USA).

Synthesis of PLGA-Pep polymers. The Pep was covalently bound to the PLGA-Mal polymers based on the Michael-type addition reaction. A cysteine was introduced to the C-terminal of the Pep to offer a thiol group that could react with the maleimide group of the PLGA-Mal polymers. Concisely, the PLGA-Mal (750 mg, 0.05 mmol) and Pep (200 mg, 0.05 mmol) were dissolved in N, N-dimethylformamide (DMF, 4 mL) and stirred overnight at room temperature. Then the final solution was purified by dialysis (Mw cutoff: 10 KDa) against deionized water and the final solution was lyophilized to obtain the PLGA-Pep polymers. The polymers were dissolved in hexadeuterodimethyl sulfoxide (DMSO-d6) and analyzed by ^{1}H NMR spectroscopy (Avance III 500, Bruker, Switzerland).

Synthesis of PLGA-PEG-Gal polymers. The PLGA-PEG-Gal polymers were synthesized by conjugating NH$_2$-PEG-Gal (Supplementary Note 4) with PLGA-COOH. The PLGA-COOH (423 mg, 0.028 mmol) was first dissolved in 2 mL DMSO, followed by adding 1-ethyl-3-(3-dimethylaminopropyl)-carbodiimide (EDC, 28 mg, 0.14 mmol) and N-hydroxysuccinimide (NHS, 16 mg, 0.14 mmol). After stirring for 15 min, the NH$_2$-PEG-Gal (34 mg, 0.028 mmol) was added and continued to react overnight. The resulting solution was purified by the method mentioned above. The obtained PLGA-PEG-Gal polymers were dissolved in DMSO-d6 and analyzed by ^{1}H NMR spectroscopy.

Preparation and characterization of nanoparticles. The nanoparticles, including PNPs, Pep-PNPs, Gal-PNPs, CPP/Gal-PNPs and Pep/Gal-PNPs, were prepared using a modified double emulsion and solvent evaporation method [47]. In brief, the functional polymers were dissolved in 2 mL of dichloromethane (DCM) as the

organic phase. Then, 0.2 mL of human insulin (dissolved in 0.01 M HCl) or aqueous sodium dodecyl sulfate (SDS, 0.05%, w/v) was emulsified with the organic phase by sonication (100 W, 30 s) to prepare the primary emulsion, which was subsequently added to 10 mL of 0.05% SDS and sonicated under the same conditions. The residual organic solvent was removed via vacuum evaporation. The nanoparticles were washed 3 times with PBS by centrifugation (10,000 rpm, 5 min) to remove unloaded insulin. The insulin was replaced with FITC-insulin to prepare FITC-labeled nanoparticles, or FITC and RITC in PBS (1 mg/mL, 50 μL) were added simultaneously to prepare FITC/RITC-labeled nanoparticles.

The size and zeta potential of nanoparticles suspended in PBS at pH 3.0, 5.0, 6.0, 6.8, 7.0, 7.4 and 8.0 were measured using a Zetasizer (Nano ZS, Malvern Instruments, UK). Nanoparticle morphology was observed by cryogenic transmission electron microscopy (cryo-TEM; TF20, FEI, USA) with an acceleration voltage of 200 kV. The entrapment efficiency (EE) and loading capacity (LC) of insulin in nanoparticles were quantified by high-performance liquid chromatography (HPLC; Agilent 1260, USA) and calculated using equations previously reported[26]. The conjugation efficiency of Gal, Pep and CPP to the surface of nanoparticles was measured using the resorcinol/sulfuric acid micromethod and BCA assay, as previously reported[29].

Detection of nanoparticles by AFM. The nanoparticles were fixed on the silica substrate using our previously reported method[48]. Then, the substrate was immersed in buffer at pH 7.4 and scanned via AFM (FastScan Bio, Bruker, Germany) using a silicon probe (Bruker, Germany) at a rate of 1 Hz (256 samples per line) at 37 °C. Then, the probe was lifted, and the medium was discarded and replaced with buffer at pH 6.8 without moving the substrate. After incubation for 10 min, the substrate was scanned repeatedly by AFM under the same conditions. For the detection of ligand corona around nanoparticles, more than 10 nanoparticles were carefully examined for each group. Height-map images were handled for 3D reconstruction and the height profiles were processed by NanoScope Analysis software (Bruker, Germany).

Cellular uptake studies on Caco-2 Cells. The Caco-2 cells were seeded on 24-well plates and cultured for 2 days. The FITC-labeled nanoparticles were diluted with PBS (pH 6.8 or 7.4) to maintain the same dose of encapsulated insulin at 20 ug/mL. The cells were incubated with FITC-labeled nanoparticles for 2 h. Then the cells were washed with PBS and disrupted by RIPA lysis buffer. The amount of insulin in the lysate was detected using the microplate reader and the total protein was quantified by

the BCA kit. For CLSM observation, the Caco-2 cells were seeded on the microscope slides for 2 days. The cells were incubated with FITC-labeled nanoparticles for 2 h. Then the cells were washed, fixed with 4% paraformaldehyde, and stained with DAPI for 10 min. The cellular uptake of nanoparticles was observed using CLSM (FV1000, Olympus, Japan).

Intracellular fate of nanoparticles. In brief, the Caco-2 cells were stained with Hoechst 33342 and Lyso-Tracker Red at 37 °C for 30 min. Then FITC-labeled nanoparticles at pH 6.8 and 7.4 were added to cells, which were incubated for another 2 h. Afterward, the colocalization signals of nanoparticles with lysosomes were imaged by CLSM.

Transcellular transport studies. To investigate the transcytosis efficiency of nanoparticles, the Caco-2 cells were seeded on the 12-well transwell plates and continuously cultured for 21 days to mimic the intestinal epithelium monolayer. The cells were incubated with FITC-labeled nanoparticles at pH 6.8 and 7.4, respectively. Then, 0.2 mL of sample from the basolateral chamber was removed at predetermined time intervals (0.5, 1, 1.5, 2 h) and an equal amount of PBS was supplemented to maintain the volume. Meanwhile, TEER values of cells were measured using an electrical resistance meter (Millicell ERS-2, Millipore). The FITC-insulin was quantified using the microplate reader and the P_{app} values of insulin in different formulations were calculated using the following equation:

$$P_{app} = \frac{dQ}{dt} \times \frac{1}{A \times C_0} \tag{1}$$

where dQ/dt is the flux of insulin from the apical to the basolateral chamber, A is the diffusion membrane area (cm^2) and C_0 is the initial concentration of insulin in the donor compartment.

FRET assays were conducted to evaluate the integrity and pH sensitivity of the Pep/Gal-PNPs after exocytosis. The FITC/RITC-labeled Pep/Gal-PNPs (FITC/RITC@NP) was incubated with Caco-2 cells at pH 6.8 for 2 h. Subsequently, the basolateral sample was collected and the FRET emission of the sample was detected at 450 nm by the microplate reader. In addition, the Pep/Gal-PNPs collected from the basolateral sample was also observed using cryo-TEM. The Edans/Dabcyl-labeled Pep was utilized to prepare Pep/Gal-PNPs (Edans-Pep-Dabcyl-NP) as desribed above. After incubation with Caco-2 cells for 2 h, the basolateral sample was collected and adjusted to pH 6.8 or 7.4, and then the emission spectra of the sample

710   were measured with an excitation wavelength at 340 nm by the microplate reader.

711   **Interaction of Pep/Gal-PNPs with hepatocytes.** LO2 cells were seeded on

712   microscope slides and cultured for 2 days. The cells were incubated with FITC-

713   labeled nanoparticles at pH 6.8 and 7.4 for 2 h. To investigate the effect of Gal on the

714   interaction of nanoparticles with cells, LO2 cells were pretreated with 50 μM Gal for

715   1 h at 37 °C before incubation with nanoparticles. Then, the cells were stained with

716   DAPI and observed by CLSM.

717   To investigate the colocalization of Pep/Gal-PNPs with ASGPRs on LO2 cells, the

718   cells were incubated with FITC-labeled Pep/Gal-PNPs at pH 6.8 and 7.4 for 2 h and

719   then stained using the anti-ASGPR rabbit pAb (diluted with 5% BSA to 1:50) as

720   primary antibody and Alexa 647-labeled goat anti-rabbit IgG (diluted with 5% BSA to

721   1:200) as the secondary antibody. The colocalization signals were imaged by CLSM.

722   **Intracellular signaling pathway studies.** LO2 cells were seeded on a 12-well plate

723   and cultured for 2 days. Then the cells were incubated with free insulin and insulin-

724   loaded Pep-Gal/PNPs with the same dose of insulin at 20 nM (5.8 ug/mL) for

725   predetermined time intervals. Afterward, the cells were washed and lysed with RIPA

726   containing protease inhibitors and phosphatase inhibitors. The expression of p-AKT in

727   cells was analyzed by western blot (Supplementary Note 11). The phospho-AKT

728   (Ser473) rabbit mAb (diluted with 5% BSA to 1:1000) was utilized as primary

729   antibody and the HRP-conjugated goat anti-rabbit IgG (diluted with 5% BSA to

730   1:5000) as secondary antibody for the detection of p-AKT in cells.

731   **Intestinal absorption studies.** To directly observe the real-time intestinal absorption

732   of nanoparticles in the living rats, the TPM was performed for intravital imaging as

733   reported previously.[33] The rats were fasted overnight before studies and then injected

734   intraperitoneally with Hoechst 33258 (2 mg/kg). After 30 min, the rats were

735   anesthetized, and the small intestine was gently pulled and stuck to the glass slide.

736   The intestinal segment was cut along one side and the FITC-labeled nanoparticles at

737   pH 6.8 and 7.4 were added respectively. Subsequently, the intestinal absorption of

738   nanoparticles along with time was detected using the TPM (Olympus, FV1200MPE,

739   Japan). The integrated densities of images were quantified using ImageJ software

740   (NIH, USA).

741   For CLSM observation, after the rats were anesthetized, about 5 cm segments of the

742   small intestine were ligated at both ends. Then the FITC/RITC-labeled nanoparticles

743   at pH 6.8 and 7.4 were injected into the loops. After treatment for 2 h, the rats were

sacrificed and the intestinal loops were excised and fixed in 4% paraformaldehyde for 4 h, then stored in 30% sucrose overnight. Afterward, the frozen sections of each loop were obtained using a cryostat (CM1950, Leica, Germany) and then stained with DAPI for 10 min. The absorption of nanoparticles in the intestinal villi was observed by CLSM.

Biodistribution studies. The rats were fasted overnight and then administered orally with PBS or FITC-labeled nanoparticles. After treatment for 4 h, the rats were sacrificed, and the major organs were isolated and examined using the IVIS spectrum system (Perkin Elmer, USA). Additionally, the organs were further sheared by a high-speed disperser (Ultra-Turrax T 25, IKA Werke, Germany), and the fluorescence intensity of tissue homogenates were detected using the microplate reader.

Liver-targeting ability studies. To detect the liver targeting ability of the nanoparticles, immunofluorescent staining was performed on the liver sections. In brief, the rats were fasted overnight before study and then administered orally with FITC-labeled nanoparticles. After treatment for 4 h, the rats were sacrificed, and the livers were isolated. Then, the frozen sections of liver were obtained using a cryostat and stained using anti-ASGPR rabbit pAb as primary antibody and Alexa 647 labeled goat anti-rabbit IgG as secondary antibody. Afterward, the liver sections were stained with DAPI and the colocalization signals of nanoparticles with ASGPRs were observed by CLSM. The colocalization coefficient (R) was quantified using Imaris software (Bitplane AG, Switzerland).

Analysis of ligand-switching features of Pep on Pep/Gal-PNPs. FAM and TAMRA (a FRET pair) were conjugated to the N- and C-termini of Pep, respectively, to prepare FR-labeled Pep. Then the PF-labeled Pep was used to prepare Pep/Gal-PNPs (FR-Pep/Gal-PNPs) as described above. The rats were fasted overnight and then orally administered with FR-Pep/Gal-PNPs at a dose of 50 mg/kg. The rats were sacrificed at either 2 h after treatment to collect a 2–3 cm segment of the duodenum or at 4 h to collect a lobe of the liver. After staining with Hoechst 33258 for 15 min, the tissues were observed by CLSM (TCS SP8, Leica, Germany), and the FRET efficiency was analyzed using the FRET acceptor photobleaching method.

Studies on the systemic delivery route of Pep/Gal-PNPs. The rat was fasted overnight and then orally administered FITC-labeled Pep/Gal-PNPs. After treatment for 2 h, the rat was anesthetized, the abdomen was exposed, and the intestine was externalized for scanning by confocal laser endomicroscopy (ViewnVivo B30,

778 OptiScan, Australia) with a z-step size of 3 μm. Subsequently, the abdominal incision

779 in rat was sutured. After treatment for an additional 2 h, the liver was scanned

780 following the same procedure.

781 **Therapeutic efficacy studies on diabetic rats.** The diabetic rats were fasted

782 overnight before studies and then administered with different formulations (each

783 group n=6): free insulin solution at a dose of 5 IU/kg via subcutaneous injection; free

784 insulin solution, insulin-loaded nanoparticles at a dose of 75 IU/kg via oral gavage.

785 The blood samples were collected from the tail veins of rats before administration and

786 at predetermined time intervals after dosing. The blood glucose level was measured

787 using the glucose meter (On Call® EZ, Acon Biotechnology).

788 To analysis peripheral serum insulin levels, the blood samples of rats were collected

789 from the eye veins before administration and at predetermined time intervals after

790 dosing. Then the blood samples were centrifuged at 4000 rpm for 10 min, and the

791 serum insulin concentrations were determined using a human insulin ELISA kit. The

792 pharmacological availability (PA%) and bioavailability (F%) of nanoparticles relative

793 to subcutaneous injection of insulin was calculated according to the following

794 equations:

795 $$PA\ (\%) = \frac{AAC_{oral} \times Dose_{s.c.}}{AAC_{s.c.} \times Dose_{oral}} \times 100\% \tag{2}$$

796 $$F\ (\%) = \frac{AUC_{oral} \times Dose_{s.c.}}{AUC_{s.c.} \times Dose_{oral}} \times 100\% \tag{3}$$

797 where AAC denotes the area above the blood glucose level versus time curve.

798 For analysis of the portal serum insulin level, the blood samples were collected from

799 the portal vein of rats by cannulation before administration and at predetermined time

800 intervals after dosing. Then the blood samples were centrifuged at 4000 rpm for 10

801 min, and the portal serum insulin concentrations were determined using the human

802 insulin ELISA kit.

803 **Hepatic glycogen measurement.** The rats were fasted overnight before studies, and

804 then the diabetic rats were subcutaneously injected of free insulin solution (5 IU/kg)

805 or administered orally with insulin-loaded nanoparticles (75 IU/kg). The normal and

806 diabetic rats administered orally with PBS were taken as positive and negative control,

807 respectively. After treatment for 4 h, the rats were fed with food. Following daily

808 dosing for one week, the rats were sacrificed to collect the livers. The hepatic

809 glycogen contents in rats were measured by the glycogen assay kit. Afterward, the

810 livers were fixed with 4% paraformaldehyde and stained using periodic acid-Schiff

(PAS) staining method. The synthesized hepatic glycogen was observed by a light microscope (DM 6B, Leica, Germany).

***In vivo* toxicity analysis.** The biocompatibility of nanoparticles was investigated following healthy rats were administrated orally with PBS and nanoparticles (1 mg/mL) every day for a week. The body weight of rats was recorded each day after dosing. Meanwhile, the blood samples of rats were collected from eye veins at 0 and 7th day of dosing, and then the serum ALT and AST levels were determined using commercial kits. The rats were sacrificed post dosing and the livers and small intestines were isolated. Afterward, the organs were fixed with 4% paraformaldehyde and embedded in paraffin, and cut for sections. After staining with hematoxylin and eosin, the histomorphology changes of organs were observed using the light microscope.

Statistical analysis. All experiments were performed in triplicate unless otherwise stated and the results are presented as mean ± standard deviation (SD). Two-tailed Student's t-test was selected to compare two groups and one-way analysis of variance (ANOVA) with Tukey's post-hoc test was conducted when comparing multiple groups in GraphPad Prism 7.0 software. The differences were considered statistically significant for p values < 0.05.

844

Contributions

T.Y., W.F., G.W. and Y.G. designed this project. T.Y. and X.J. performed all experiments, collected, and analyzed the data. T.Y., D.N. and A.W. wrote the manuscript. T.Y., A.W., D.N., W.F., M.Y., S.G., C.Z., G.W. and Y.G. contributed to reviewing the manuscript, and discussed the results and implications.
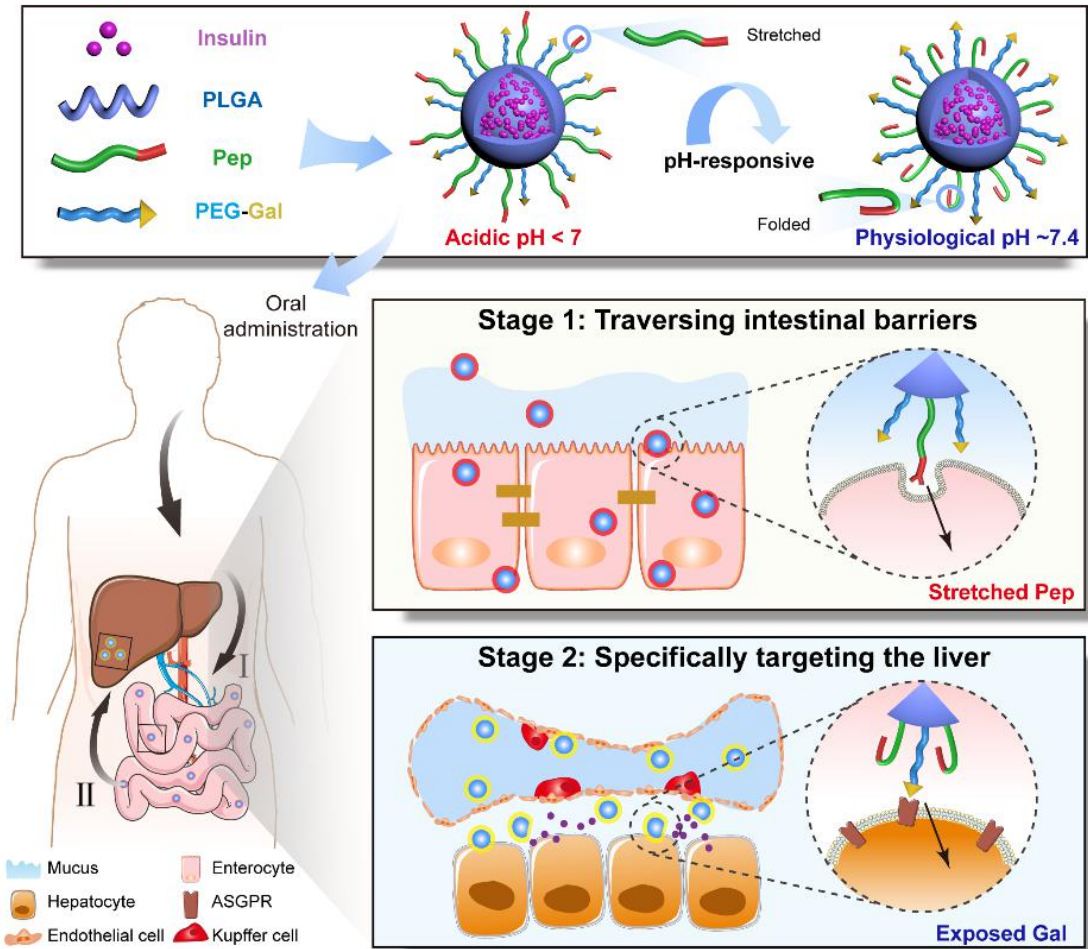
850

Ethics Declarations

The authors declare no competing interests.

853

Data Availability

The data that support the findings of this study are available within the article and its Supplementary Information files.

857

858

Figure 1. The construction of virus surface-inspired ligand-switchable nanoparticles (Pep/Gal-PNPs) modified with both a pH-triggered stretchable cell-penetrating peptide (Pep) and a hepatic targeting moiety (galactose, Gal). After oral administration, Pep adopts a stretched conformation in response to the acidic environment in the intestine and mediates efficient Pep/Gal-PNPs transport across intestinal barriers. Subsequently, Gal is exposed on the surface as Pep folds at physiological pH in circulation and specifically guides Pep/Gal-PNPs to the liver.
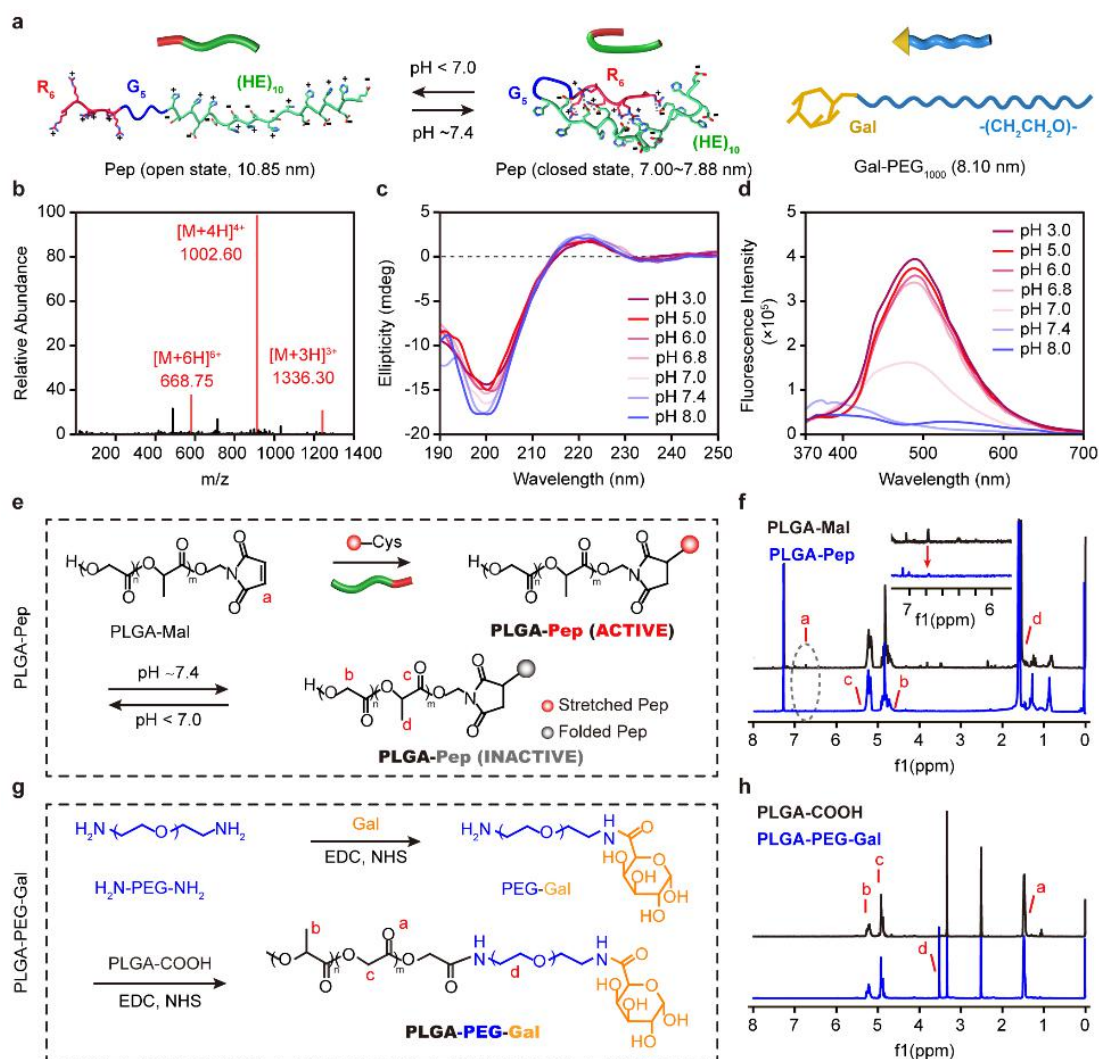
Figure 2. Synthesis and characterization of functional polymers. (a) Schematic illustration of pH-responsive stretchable cell-penetrating peptide (Pep) and polyethylene glycol-galactose (PEG-Gal) polymers and their theoretical lengths. Open- and closed-state models of Pep under different pH conditions. H: histidine; E: glutamic acid; G: glycine; R: arginine. (b) Mass spectrum of Pep. (c) Circular dichroism spectra of Pep and (d) emission spectra of FRET pair-labeled Pep under different pH conditions. (e) The synthetic route to PLGA-Pep polymers. (f) ^{1}H NMR spectra of PLGA-Mal and PLGA-Pep polymers. Characteristic peaks are assigned according to the labels in panel (e). (g) The synthetic route to PLGA-PEG-Gal polymers. (h) ^{1}H NMR spectra of PLGA-COOH and PLGA-PEG-Gal polymers. Characteristic peaks are assigned according to the labels in panel (g).

878
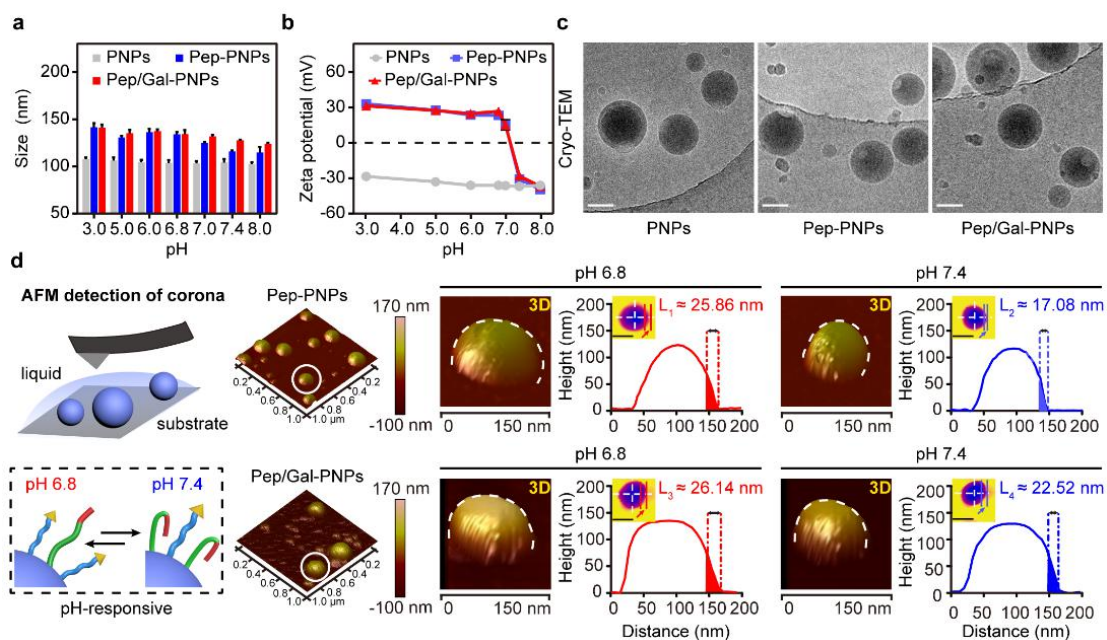
Figure 3. Synthesis and characterization of Pep/Gal-PNPs. (a) The size and (b) zeta potential of nanoparticles under different pH conditions. Data are presented as the mean ± SD (n=3). (c) Cryo-TEM images of nanoparticles. Scale bar: 100 nm. (d) Atomic force microscopy (AFM) analysis of nanoparticles under fluid conditions. 3D modeling images, height maps and height profiles of Pep-PNPs (top row) and Pep/Gal-PNPs (bottom row) at pH 6.8 and 7.4. Scale bar: height map, 100 nm. The thickness of ligand corona around the nanoparticles (as indicated by the arrows in the height map) was analyzed using NanoScope Analysis software. Representative images are presented and the data are means ± SD (n=3).

Step 1. Pep-mediated transcytosis

Step 2. Gal-mediated targeting
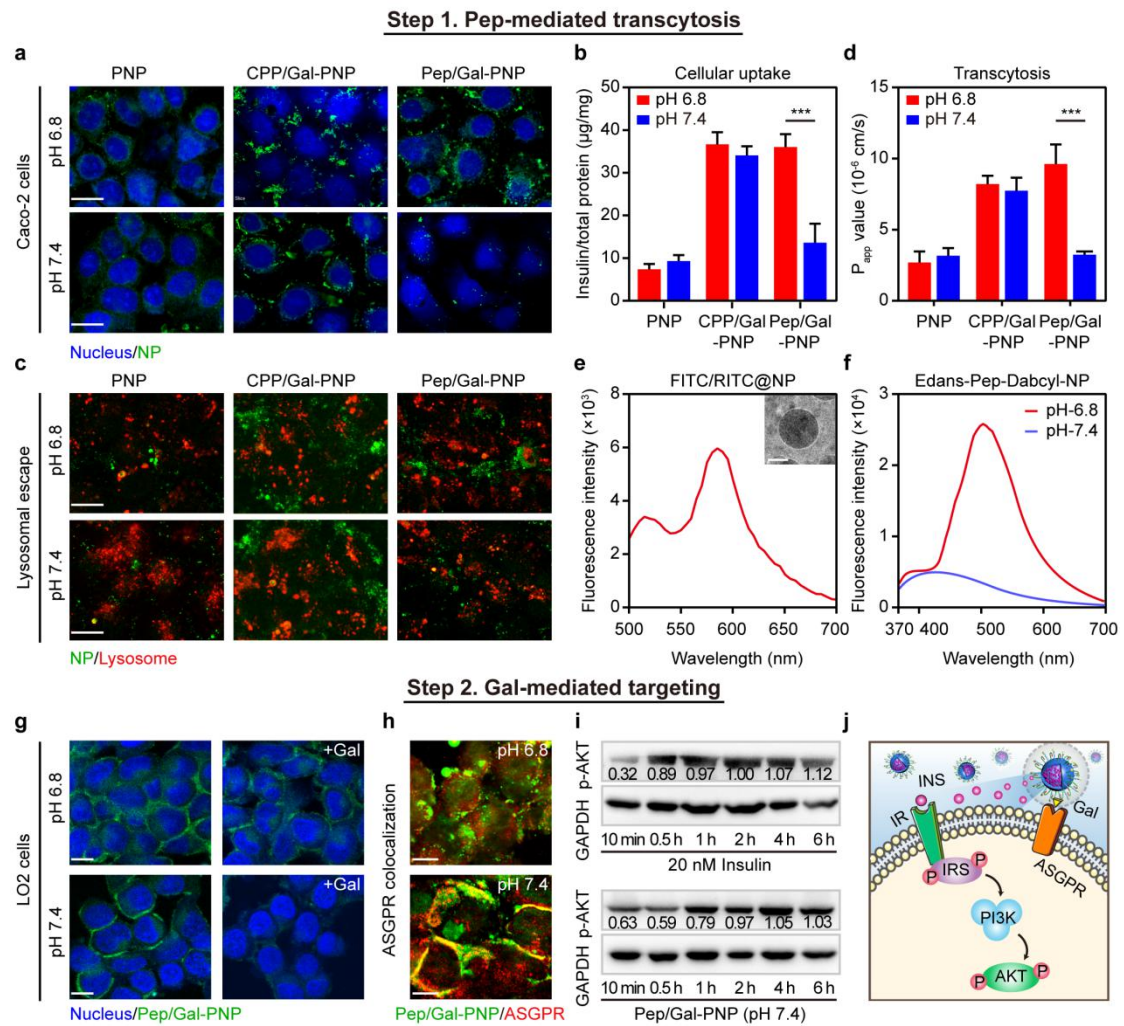
888

889 **Figure 4. *In vitro* transepithelial transport and hepatocyte selectivity of Pep/Gal-**

890 **PNPs.** (a) Cellular uptake of nanoparticles by Caco-2 cells. Scale bar: 10 μm. (b)

891 Quantitative analysis of nanoparticles internalized by Caco-2 cells. Data are presented

892 as the mean ± SD (n=3). ***$p < 0.001$ compared with the pH 7.4 group. (c) Confocal

893 laser scanning microscopy (CLSM) images of the colocalization of nanoparticles with

894 lysosomes. Scale bar: 10 μm. (d) Apparent permeability coefficient (P_{app}) values for

895 nanoparticle transport across Caco-2 cells. Data are presented as the mean ± SD (n=3).

896 ***$p < 0.001$ compared with the pH 7.4 group. (e) Emission spectrum and cryo-TEM

897 image of FITC/RITC-loaded Pep/Gal-PNPs (FITC/RITC@NP) collected from the

898 basolateral medium. Scale bar: 100 nm. (f) Emission spectra of Edans/Dabcyl-labeled

899 Pep-modified Pep/Gal-PNPs (Edans-Pep-Dabcyl-NP) collected from the basolateral

900 medium at different pH values. (g) CLSM images of Pep/Gal-PNPs binding to LO2

901 cells. +Gal: in the presence of free galactose. Scale bar: 10 μm. (h) The colocalization

902 of Pep/Gal-PNPs with ASGPRs on LO2 cells at different pH values. Scale bar: 10 μm.

903 (i) Western blot analysis of p-AKT levels in LO2 cells after incubation with free

insulin or insulin-loaded Pep/Gal-PNPs at pH 7.4 for the indicated time. The numbers represent the quantitative results of p-AKT levels normalized to GAPDH levels. (j) Schematic illustration of signaling in LO2 cells after exposure to Pep/Gal-PNPs at physiological pH.
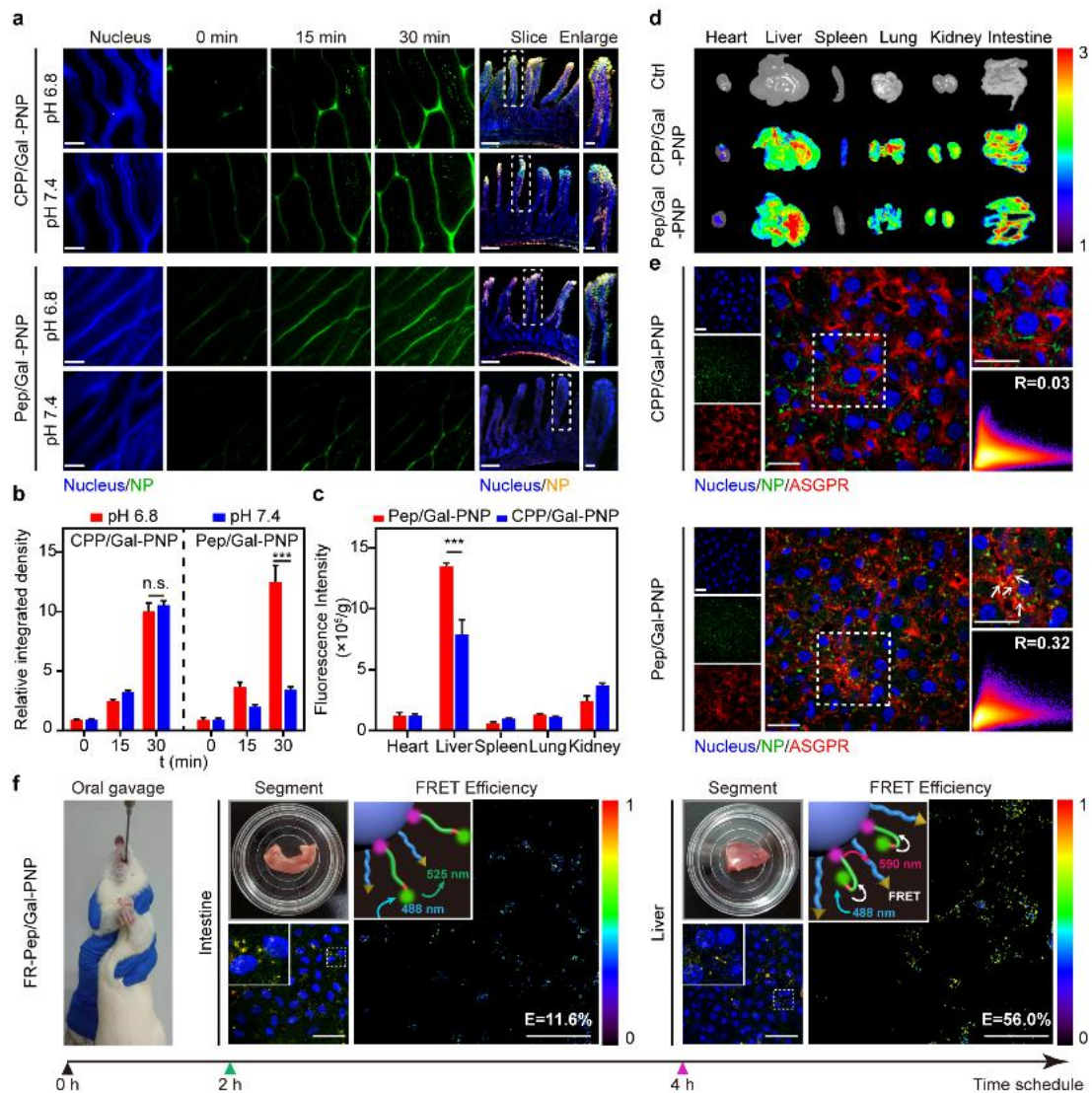
Figure 5. *In vivo* **sequential intestinal absorption and liver accumulation of Pep/Gal-PNPs.** (a) Two-photon microscopy (TPM) images show the absorption of nanoparticles in intestinal villi. Scale bar: 100 μm. Confocal laser scanning microscopy (CLSM) images of intestinal villus sections. Scale bars: intestinal slice images, 200 μm; enlarged images, 50 μm. (b) Quantitative analysis of the absorption of nanoparticles in intestinal villi. Data are presented as the mean ± SD (n=3). ***$p <$ 0.001, n.s., not significant, compared with the pH 7.4 group. (c) The fluorescence intensity of different tissue homogenates prepared from rats 4 h after the oral administration of FITC-labeled nanoparticles. Data are presented as the mean ± SD (n=3). ***$p <$ 0.001 compared with the CPP/Gal-PNP group. (d) The accumulation of nanoparticles in major rat organs as imaged by *in vivo* imaging system (IVIS). Ctrl: rats treated with PBS. The color bar indicates the radiant efficiency $\times 10^7$ p/sec/cm^2/sr. (e) The colocalization of nanoparticles with ASGPRs in liver sections. R:

33

922 colocalization coefficient. Scale bar: 20 μm. (f) The distribution and FRET efficiency

923 of FAM/TAMRA-labeled Pep-modified Pep/Gal-PNPs (FR-Pep/Gal-PNPs) in

924 intestine and liver segments prepared from rats 2 h and 4 h after oral administration,

925 respectively.
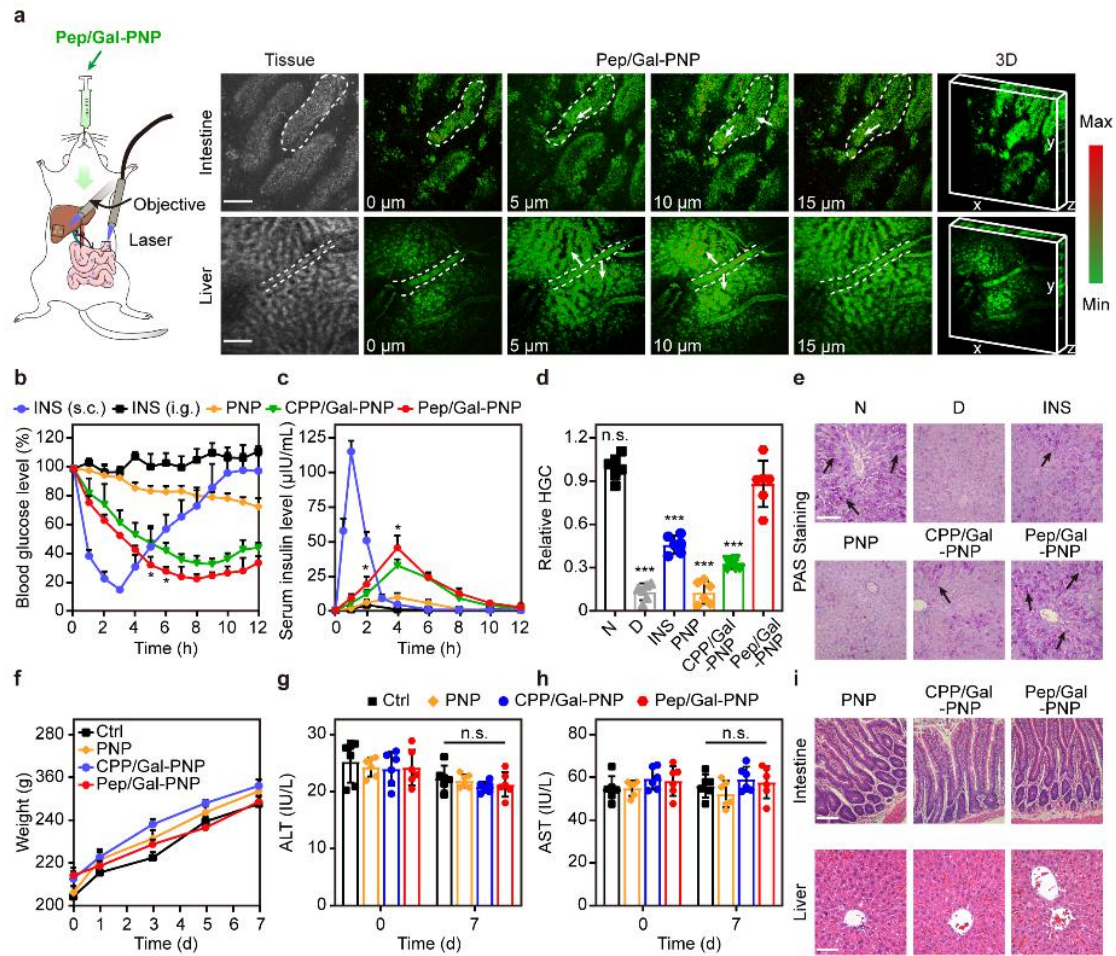
Figure 6. *In vivo* trafficking, hypoglycemic effects, and toxicity of nanoparticles. (a) Confocal laser endomicroscopy (CLE) images of intestine villi (top row) and liver lobe (bottom row) from a rat obtained 2 h and 4 h, respectively, after oral administration of FITC-labeled Pep/Gal-PNPs. The color bar indicates the fluorescence intensity. Scale bar: 100 μm. (b) Blood glucose levels over time in type I diabetic rats following oral administration of insulin (INS, i.g., 75 IU/kg), insulin-loaded nanoparticle formulations (PNP, CPP/Gal-PNP and Pep/Gal-PNP, i.g., 75 IU/kg) and subcutaneous injection of insulin (INS, s.c., 5 IU/kg). Data are presented as the mean ± SD (n=6). *$p < 0.05$ compared with the CPP/Gal-PNP group. (c) Peripheral serum insulin levels over time in diabetic rats treated with different formulations. Data are presented as the mean ± SD (n=6). *$p < 0.05$ compared with the CPP/Gal-PNP group. (d) Relative hepatic glycogen content (HGC) in healthy rats treated with PBS (N); diabetic rats treated with PBS (D), insulin (INS, s.c., 5 IU/kg), and insulin-loaded nanoparticle formulations (PNP, CPP/Gal-PNP, and Pep/Gal-PNP, i.g., 75 IU/kg). Data are presented as the mean ± SD (n=6). ***$p < 0.001$, n.s., not significant compared with the Pep/Gal-PNP group. (e) Images of periodic acid-Schiff

35

943   (PAS) staining of liver sections from healthy and diabetic rats treated with different

944   formulations. The black arrows denote synthesized glycogen. Scale bar: 100 μm. (f)

945   Average body weight of healthy rats treated with PBS (Ctrl) and nanoparticle

946   formulations (PNP, CPP/Gal-PNP, and Pep/Gal-PNP, i.g., 1000 mg/kg) every day for

947   a week. Data are presented as the mean ± SD (n=6). (g) Serum ALT and (h) AST

948   levels in rats treated with different formulations. Data are presented as the mean ± SD

949   (n=6). n.s., not significant compared with the Ctrl group. (i) Images of hematoxylin

950   and eosin (H&E) staining of intestine and liver sections from rats treated with

951   different formulations. Scale bar: 100 μm.

952 **Table 1. Pharmacokinetic parameters of different insulin formulations following**
953 **oral or subcutaneous administration to diabetic rats.** Data are presented as the
954 mean ± SD (n=6).

	Insulin (s.c.)	Insulin (i.g.)	PNP (i.g.)	CPP/Gal-PNP (i.g.)	Pep/Gal-PNP (i.g.)
Dose (IU/kg)	5	75	75	75	75
AUC (μIU*h/mL)[a]	182.2 ± 7.1	11.0 ± 1.0	41.6 ± 6.0	159.4 ± 10.4	210.6 ± 14.9
T_{max} (h)[b]	1	4	4	4	4
F (%)[c]	100	0.4	1.5	5.8	7.7

955 [a] AUC: area under the peripheral serum insulin level versus time curve; [b] T_{max}: time at
956 which the maximum plasma insulin level was reached; [c] F: relative bioavailability. s.c.,
957 subcutaneous; i.g., intragastric (oral).

References

959   1.   Mi, P., Cabral, H. & Kataoka, K. Ligand-installed nanocarriers toward
960   precision therapy. *Adv. Mater.* **32,** e1902604 (2020).

961   2.   Zhu, Y., Feijen, J. & Zhong, Z. Dual-targeted nanomedicines for enhanced
962   tumor treatment. *Nano Today* **18,** 65-85 (2018).

963   3.   Xu, Q. et al. Anti-tumor activity of paclitaxel through dual-targeting carrier of
964   cyclic RGD and transferrin conjugated hyperbranched copolymer
965   nanoparticles. *Biomaterials* **33,** 1627-1639 (2012).

966   4.   Liu, M. et al. Combinatorial entropy behaviour leads to range selective
967   binding in ligand-receptor interactions. *Nat. Commun.* **11,** 4836 (2020).

968   5.   Xia, Q., Ding, H. & Ma, Y. Can dual-ligand targeting enhance cellular uptake
969   of nanoparticles? *Nanoscale* **9,** 8982-8989 (2017).

970   6.   Colombo, M. et al. Tumour homing and therapeutic effect of colloidal
971   nanoparticles depend on the number of attached antibodies. *Nat. Commun.* **7,**
972   13818 (2016).

973   7.   Sawant, R. R., Jhaveri, A. M., Koshkaryev, A., Qureshi, F. & Torchilin, V. P.
974   The effect of dual ligand-targeted micelles on the delivery and efficacy of
975   poorly soluble drug for cancer therapy. *J. Drug Targeting* **21,** 630-638 (2013).

976   8.   Zhu, X. et al. Sub-50 nm nanoparticles with biomimetic surfaces to
977   sequentially overcome the mucosal diffusion barrier and the epithelial
978   absorption barrier. *Adv. Funct. Mater.* **26,** 2728-2738 (2016).

979   9.   Liu, Y. et al. Synergetic combinations of dual-targeting ligands for enhanced in
980   vitro and in vivo tumor targeting. *Adv. Healthcare Mater.* **7,** e1800106 (2018).

981   10.   Zhu, L., Kate, P. & Torchilin, V. P. Matrix metalloprotease 2-responsive
982   multifunctional liposomal nanocarrier for enhanced tumor targeting. *ACS*
983   *Nano* **6,** 3491-3498 (2012).

984   11.   Mura, S., Nicolas, J. & Couvreur, P. Stimuli-responsive nanocarriers for drug
985   delivery. *Nat. Mater.* **12,** 991 (2013).

986   12.   Zhao, B. et al. The efficiency of tumor-specific pH-responsive peptide-
987   modified polymeric micelles containing paclitaxel. *Biomaterials* **33,** 2508-
988   2520 (2012).

989   13.   Lee, E. S. et al. Super pH-sensitive multifunctional polymeric micelle for
990   tumor pHe specific TAT exposure and multidrug resistance. *J. Controlled*

Release **129,** 228-236 (2008).

14. Song, X. et al. Cryo-EM analysis of the HCoV-229E spike glycoprotein reveals dynamic prefusion conformational changes. *Nat. Commun.* **12,** 141 (2021).

15. De Vries, E., Du, W., Guo, H. & De Haan, C. A. M. Influenza A virus hemagglutinin-neuraminidase-receptor balance: preserving virus motility. *Trends Microbiol.* **28,** 57-67 (2020).

16. Harrison, S. C. Viral membrane fusion. *Nat. Struct. Mol. Biol.* **15,** 690-698 (2008).

17. Benton, D. J., Gamblin, S. J., Rosenthal, P. B. & Skehel, J. J. Structural transitions in influenza haemagglutinin at membrane fusion pH. *Nature* **583,** 150-153 (2020).

18. Kim, I. S. et al. Mechanism of membrane fusion induced by vesicular stomatitis virus G protein. *Proc. Natl. Acad. Sci. U. S. A.* **114,** E28-E36 (2017).

19. Walls, A. C. et al. Tectonic conformational changes of a coronavirus spike glycoprotein promote membrane fusion. *Proc. Natl. Acad. Sci. U. S. A.* **114,** 11157-11162 (2017).

20. Wang, A. et al. Liver-target and glucose-responsive polymersomes toward mimicking endogenous insulin secretion with improved hepatic glucose utilization. *Adv. Funct. Mater.* **30,** 1910168 (2020).

21. Tang, B. et al. Acid-sensitive hybrid polymeric micelles containing a reversibly activatable cell-penetrating peptide for tumor-specific cytoplasm targeting. *J. Controlled Release* **279,** 147-156 (2018).

22. Bustamante, A. et al. The energy cost of polypeptide knot formation and its folding consequences. *Nat. Commun.* **8,** 1581 (2017).

23. Reeb, J. & Rost, B. Secondary Structure Prediction. *Encyclopedia of Bioinformatics and Computational Biology* **2,** 488-496 (Academic Press, Oxford, 2019).

24. Haggag, Y. et al. Preparation and in vivo evaluation of insulin-loaded biodegradable nanoparticles prepared from diblock copolymers of PLGA and PEG. *Int. J. Pharm.* **499,** 236-246 (2016).

25. Zaro, J. L., Fei, L. & Shen, W. C. Recombinant peptide constructs for targeted cell penetrating peptide-mediated delivery. *J. Controlled Release* **158,** 357-361 (2012).

1025 26. Wang, A. et al. Protein corona liposomes achieve efficient oral insulin delivery
1026   by overcoming mucus and epithelial barriers. *Adv. Healthcare Mater.* **8,**
1027   e1801123 (2019).

1028 27. Behzadi, S. et al. Cellular uptake of nanoparticles: journey inside the cell.
1029   *Chem. Soc. Rev.* **46,** 4218-4244 (2017).

1030 28. Bus, T., Traeger, A. & Schubert, U. S. The great escape: how cationic
1031   polyplexes overcome the endosomal barrier. *J. Mater. Chem. B.* **6,** 6904-6918
1032   (2018).

1033 29. Liu, L. et al. A novel galactose-PEG-conjugated biodegradable copolymer is
1034   an efficient gene delivery vector for immunotherapy of hepatocellular
1035   carcinoma. *Biomaterials* **184,** 20-30 (2018).

1036 30. Edgerton, D. S. et al. Targeting insulin to the liver corrects defects in glucose
1037   metabolism caused by peripheral insulin delivery. *JCI Insight* **5,** e126974
1038   (2019).

1039 31. Molinaro, A. et al. Insulin-Driven PI3K-AKT Signaling in the Hepatocyte Is
1040   Mediated by Redundant PI3Kα and PI3Kβ Activities and Is Promoted by RAS.
1041   *Cell Metab.* **29,** 1400-1409 (2019).

1042 32. Liu, Y., Wang, H. Y., Shao, J., Zaro, J. L. & Shen, W. C. Enhanced insulin
1043   receptor interaction by a bifunctional insulin-transferrin fusion protein: an
1044   approach to overcome insulin resistance. *Sci. Rep.* **10,** 7724 (2020).

1045 33. Fan, W. et al. Functional nanoparticles exploit the bile acid pathway to
1046   overcome multiple barriers of the intestinal epithelium for oral insulin delivery.
1047   *Biomaterials* **151,** 13-23 (2018).

1048 34. Zhang, Y., Poon, W., Tavares, A. J., McGilvray, I. D. & Chan, W.
1049   Nanoparticle-liver interactions: cellular uptake and hepatobiliary elimination.
1050   *J. Controlled Release* **240,** 332-348 (2016).

1051 35. Asif, M. The prevention and control the type-2 diabetes by changing lifestyle
1052   and dietary pattern. *J Educ Health Promot* **3,** 1 (2014).

1053 36. Chen, M. C., Sonaje, K., Chen, K. J. & Sung, H. W. A review of the prospects
1054   for polymeric nanoparticle platforms in oral insulin delivery. *Biomaterials* **32,**
1055   9826-9838 (2011).

1056 37. Hasan, K. M. M., Tamanna, N. & Haque, M. A. Biochemical and
1057   histopathological profiling of Wistar rat treated with Brassica napus as a
1058   supplementary feed. *Food Sci. Hum. Wellness* **7,** 77-82 (2018).

1059   38.   Maslanka Figueroa, S., Fleischmann, D. & Goepferich, A. Biomedical
1060   nanoparticle design: what we can learn from viruses. *J. Controlled Release*
1061   **329,** 552-569 (2020).

1062   39.   Drucker, D. J. Advances in oral peptide therapeutics. *Nat. Rev. Drug Discov.*
1063   **19,** 277-289 (2020).

1064   40.   Xiao, Y. et al. Oral insulin delivery platforms: strategies to address the
1065   biological barriers. *Angew. Chem. Int. Ed. Engl.* **59,** 19787-19795 (2020).

1066   41.   Sharma, R. et al. Rationally designed galactose dendrimer for hepatocyte-
1067   specific targeting and intracellular drug delivery for the treatment of liver
1068   disorders. *Biomacromolecules* **22,** 3574-3589 (2021).

1069   42.   Geho, W. B. The importance of the liver in insulin replacement therapy in
1070   insulin-deficient diabetes. *Diabetes* **63,** 1445-1447 (2014).

1071   43.   Edgerton, D. S., Moore, M. C., Gregory, J. M., Kraft, G. & Cherrington, A. D.
1072   Importance of the route of insulin delivery to its control of glucose metabolism.
1073   *Am. J. Physiol.: Endocrinol. Metab.* **320,** E891-E897 (2021).

1074   44.   Li, Q. et al. The protein phosphatase 1 complex is a direct target of AKT that
1075   links insulin signaling to hepatic glycogen deposition. *Cell Rep.* **28,** 3406-
1076   3422.e7 (2019).

1077   45.   Arbit, E. & Kidron, M. Oral insulin delivery in a physiologic context: Review.
1078   *J. Diabetes Sci. Technol.* **11,** 825-832 (2017).

1079   46.   Winnick, J. J. et al. Hepatic glycogen can regulate hypoglycemic
1080   counterregulation via a liver-brain axis. *J. Clin. Invest.* **126,** 2236-2248 (2016).

1081   47.   Cohen-Sela, E., Chorny, M., Koroukhov, N., Danenberg, H. D. & Golomb, G.
1082   A new double emulsion solvent diffusion technique for encapsulating
1083   hydrophilic molecules in PLGA nanoparticles. *J. Controlled Release* **133,** 90-
1084   95 (2009).

1085   48.   Wei, Y. et al. MT1-MMP-activated liposomes to improve tumor blood
1086   perfusion and drug delivery for enhanced pancreatic cancer therapy. *Adv. Sci.*
1087   *(Weinheim, Ger.)* **7,** 1902746 (2020).

1088

Supplementary Files

This is a list of supplementary files associated with this preprint. Click to download.

- Supportinginformation.pdf